Materials Science & Engineering A 950 (2026) 149539

Contents lists available at ScienceDirect

Materials Science & Engineering A

journal homepage: www.elsevier.com/locate/msea

Effects of prior austenite grain size on hydrogen embrittlement behavior in high-strength martensitic steel

Xiaodong Lan *, Kazuho Okada, Ivan Gutierrez-Urrutia, Akinobu Shibata

Research Center for Structural Materials, National Institute for Materials Science, 1-2-1 Sengen, Tsukuba, Ibaraki, 305-0047, Japan

ARTICLE INFO

Keywords:
Martensitic steel
Hydrogen embrittlement
Prior austenite grain size
Crack morphology
Three-dimensional analysis

ABSTRACT

The present study investigates the effects of prior austenite grain (PAG) size on hydrogen embrittlement behavior in high-strength martensitic steel utilizing slow strain rate tensile tests integrated with digital image correlation (DIC) and X-ray computed tomography analyses. The results demonstrate that PAG refinement significantly improves the hydrogen embrittlement resistance under a similar hydrogen level. DIC analysis reveals that the susceptibility to hydrogen embrittlement originates from the plastic deformation related to the lath martensite microstructure. PAG refinement mitigates the microstructure-related strain localization, thereby enhancing the hydrogen embrittlement resistance. Additionally, PAG refinement increases the apparent fracture toughness by promoting greater plastic work and enhancing crack meandering/branching, though the latter effect peaks at a medium PAG size. The enhanced resistance to hydrogen embrittlement thus could be attributed to several factors: reduced strain localization, lower local hydrogen concentration per unit area of PAG boundaries, frequent deflection of intergranular cracks, and an increased density of high-angle boundaries that impede quasi-cleavage cracks—all facilitated by PAG refinement.

1. Introduction

Recent global decarbonization initiatives and the rapid expansion of hydrogen industry have driven a surge in need for high-strength steels [1,2]. However, high-strength steels—particularly martensitic steels—demonstrate high susceptibility to hydrogen embrittlement, a long-standing concern in the steel industry [3]. The inherent trade-off relationship between strength and hydrogen embrittlement [4], combined with the inevitable hydrogen uptake during steel manufacturing and service, poses a critical challenge in designing high-strength steels for hydrogen-rich environments.

Lath martensite, commonly found in high-strength low- and medium-carbon steels, exhibits a hierarchical arrangement of structural units—including lath, block, packet, and prior austenite grain (PAG)—governed by the Kurdjumov–Sachs orientation relationship [5–7]. As the smallest structural unit, a lath corresponds to a heavily dislocated single martensite crystal (~200 nm thick [8]). Laths having nearly identical crystallographic orientation aggregate into a block, while multiple blocks sharing a common habit plane—separated primarily by high-angle boundaries—assemble into a packet within each PAG. Hydrogen embrittlement in martensitic steels is closely associated with their substructural and crystallographic features. Although the high dislocation density and abundant high-angle martensitic boundaries give rise to the high strength of lath martensite [9], these features concurrently elevate the risk of hydrogen embrittlement. Since hydrogen embrittlement originates from hydrogen-lattice defects (e.g., vacancies, dislocations, and boundaries) interactions that promote crack initiation and propagation [10–12], understanding how martensitic microstructures influence hydrogen-related fracture is crucial for enhancing resistance to hydrogen embrittlement.

Martensitic steels typically display two hydrogen-induced fracture modes: quasi-cleavage and intergranular. Quasi-cleavage fractures propagate along non-typical cleavage planes within the martensite laths [13,14], whereas intergranular fractures predominantly proceed along prior austenite grain boundaries (PAGBs) [15–18]. Increasing hydrogen content in a given material generally shifts the fracture mode from quasi-cleavage to intergranular, thereby exacerbating brittleness [19]. Although multiple embrittlement mechanisms have been proposed, the dominant mechanism in a specific case can be influenced by various material parameters, such as strength, microstructure (e.g., grain size and chemical heterogeneity), dislocation density, hydrogen absorption capability, etc. To date, developing martensitic steels that combine high

* Corresponding author.
E-mail address: LAN.Xiaodong@nims.go.jp (X. Lan).

https://doi.org/10.1016/j.msea.2025.149539
Received 31 May 2025; Received in revised form 18 November 2025; Accepted 28 November 2025
Available online 29 November 2025

hydrogen embrittlement resistance with excellent mechanical performance remains challenging. Current strategies, such as hydrogen-blocking coatings [20], often fail under abrasive/corrosive conditions. Microstructure design has emerged as a promising alternative. For instance, Depover et al. [21] showed that microalloying martensitic steels to form TiC hydrogen-trapping precipitates can suppress internal hydrogen migration, albeit at increased cost. Okada et al. [22,23] revealed that introducing carbon segregation at PAGBs in martensitic steels reduces hydrogen embrittlement susceptibility, yet the effectiveness of this strategy is confined to relatively low hydrogen levels. In another approach, Gomes da Silva et al. [24] demonstrated that PAG refinement improves the hydrogen embrittlement resistance of maraging steels. Cho et al. [25,26] further revealed that high-angle martensitic boundaries deflect quasi-cleavage cracks and that PAG refinement both reduces the quasi-cleavage fracture area and promotes crack deflection, thereby delaying crack propagation. Most recently, Chen et al. [27] also confirmed that PAG refinement promotes crack-tip blunting and deflection in tempered martensite. Additionally, Shibata et al. [17,28,29] found that hydrogen-related intergranular cracks propagate discontinuously along PAGBs, with low-angle PAGB segments exhibiting high crack-arrestability. Collectively, these studies highlight PAG refinement as a viable strategy to improve hydrogen embrittlement resistance without altering chemical composition.

Despite these advances, most studies rely on slow strain rate tensile tests (SSRT) and postmortem two-dimensional (2D) crystallographic/fractographic analyses [24–27], which cannot quantitatively analyze the macroscopic three-dimensional (3D) crack propagation and crack-arrestability because critical features may be absent from the examined plane. As a result, a significant gap remains between microstructure and macroscopic hydrogen-related fracture characteristics. To bridge this gap, our study integrates SSRT with digital image correlation (DIC) and X-ray computed tomography (X-ray CT) to quantitatively correlate PAG size with strain localization and macroscopic crack propagation in the presence of hydrogen, thereby linking microstructure to overall mechanical performance. To our knowledge, this is the first attempt to apply these techniques to the study of hydrogen

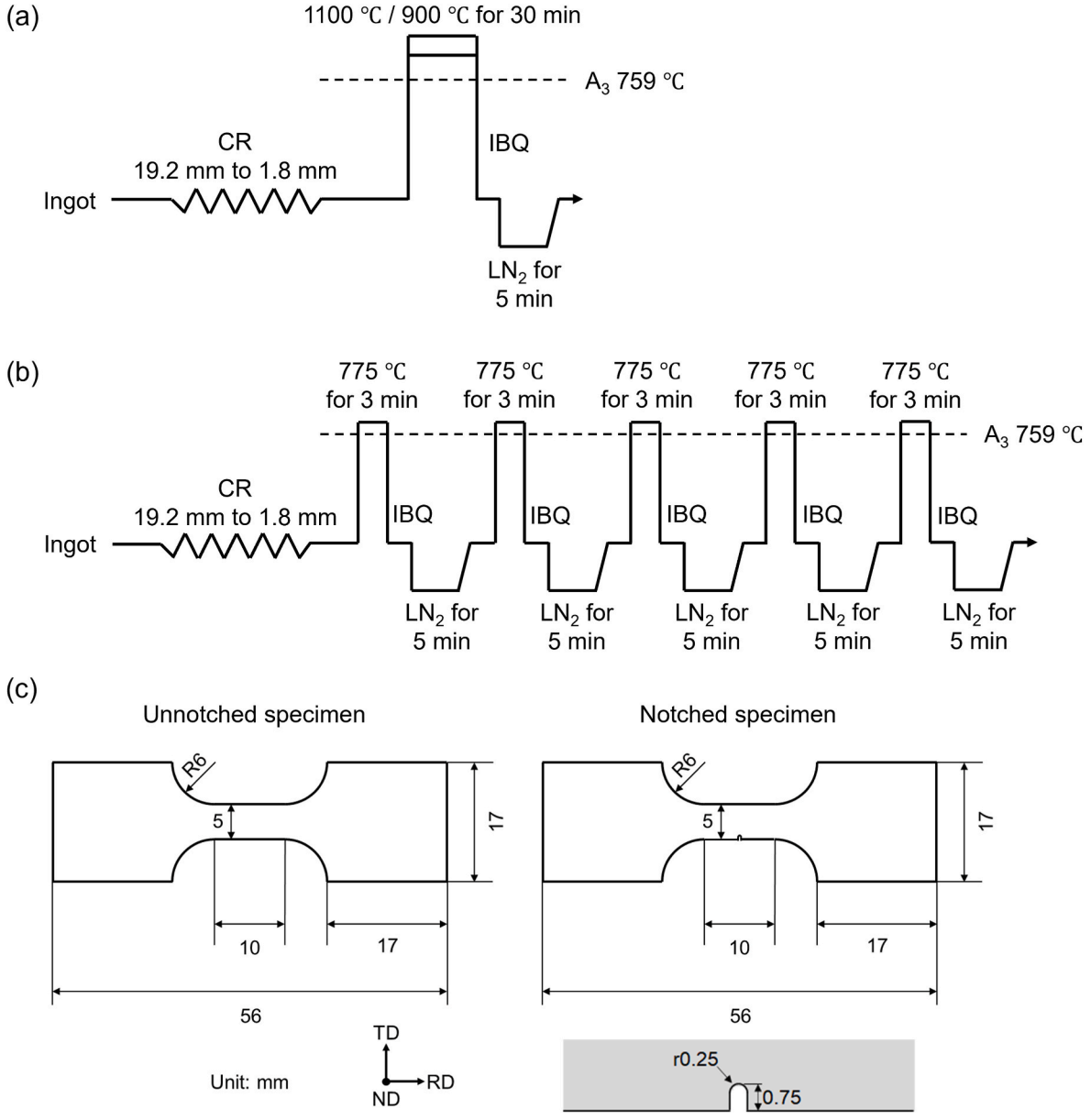

Fig. 1. Schematic diagrams of the thermomechanical processing routes: (a) one-step austenitizing and quenching, (b) repetitive austenitizing and quenching; (c) schematic diagrams of unnotched and notched tensile-test specimens.

embrittlement, providing new quantitative mechanistic insight into the underlying mechanisms through an innovative multimodal methodology that advances beyond conventional approaches.

2. Experimental

A ternary Fe-3Mn-0.2C (wt. %) alloy was used in this study. The detailed chemical composition is identical to that reported in our previous work [30]. The as-received ingot was cold-rolled from 19.2 mm to 1.8 mm (91 % thickness reduction) and then subjected to two distinct heat-treatment routes (Fig. 1(a and b)) to produce fully martensitic microstructures with different average PAG sizes. One route is one-step austenitizing and quenching (Fig. 1(a)): the cold-rolled sheets were austenitized at 1100 °C or 900 °C for 30 min, immediately ice-brine quenched, and then held in liquid nitrogen (LN_2) for 5 min. This processing route is for fabricating specimens with coarse and medium PAGs. The other route involves repetitive austenitizing and quenching (Fig. 1 (b)): the cold-rolled sheets were first heat-treated at 775 °C (slightly above A_3 temperature, 759 °C) in a salt bath for 3 min to form austenite, then ice-brine quenched and immersed in LN_2 for 5 min; such a rapid austenitizing and quenching process was referred to as one thermal cycle, and five cycles were applied to the specimens. The gains were refined through repetitive austenite ↔ martensite transformations [31, 32]. The specimens heat-treated at 1100 °C, 900 °C, and those subjected to five thermal cycles are hereafter referred to as coarse-grained (CG), medium-grained (MG), and fine-grained (FG) specimens, respectively.

The microstructures of the thermomechanically processed specimens were characterized using optical microscopy (OM), backscattered electron (BSE) imaging, and electron backscatter diffraction (EBSD) in a ZEISS Sigma scanning electron microscope (SEM) equipped with a Bruker QUANTAX EBSD system. Prior to microstructural observations, these specimens were mechanically polished using SiC grinding papers, then electrolytically polished in a 10 % $HClO_4$ + 90 % CH_3COOH solution, and finally chemo-mechanically polished with a 0.02 μm colloidal silica suspension to obtain a mirror finish. The specimens for OM were etched in saturated picric acid to expose PAGBs and in 3 % nital solution to reveal microstructural features.

Sheet-type tensile-test specimens (unnotched and notched, as shown in Fig. 1(c)), extracted from the heat-treated sheets via electrical discharge machining, were mechanically polished to about 1 mm thickness to remove heat-treatment-induced surface decarburization and finished by electrolytic polishing. The specimens for hydrogen analysis and tensile testing were pre-charged at room temperature for 24 h in an aqueous solution containing 3 % NaCl and 3 g L^{-1} NH_4SCN, with a platinum wire serving as the counter electrode. The total hydrogen uptake was controlled by varying the current density (0.5, 1, and 1.5 A m^{-2}). The diffusible hydrogen content (H_D) was measured by thermal desorption spectroscopy (TDS) using an R-DEC HTDS-004 system. The specimens were heated from room temperature to 800 °C at a rate of 100 °C h^{-1}, and the H_D was defined as the cumulative hydrogen amount desorbed between room temperature and 300 °C. The mechanical performance of specimens having different H_D was evaluated by SSRT (initial strain rate: 8.3 × 10^{-6} s^{-1}) at room temperature. To ensure reliability and reproducibility, two tensile specimens for each condition were tested. Both SSRT and TDS measurements started 30 min after hydrogen pre-charging was completed. The fracture morphologies after SSRT were examined by SEM.

Interrupted tensile tests, combined with DIC and X-ray CT (Zeiss: Xradia 620 Versa), were performed on single-edge notched tension specimens (Fig. 1(c)) to evaluate the effects of PAG size on strain localization behavior and macroscopic 3D crack propagation morphology. The U-shaped notch has a depth of 0.75 mm and a curvature radius of 0.25 mm. These tensile tests were stopped at the onset of macroscopic cracking and immediately unloaded. The apparent fracture toughness (K_Q) was calculated as [33]:

$$K_Q = \frac{P}{B\sqrt{W}} f\left(\frac{a}{W}\right) \tag{1}$$

$$f\left(\frac{a}{W}\right) = \frac{\sqrt{2\tan(\pi a/2W)}}{\cos(\pi a/2W)}\left[0.752 + 2.02\left(\frac{a}{W}\right) + 0.37\left(1 - \sin\frac{\pi a}{2W}\right)^3\right] \tag{2}$$

where P represents the applied load and $f(a/W)$ is a dimensionless geometry function. The symbols B, W, and a refer to the specimen's thickness, width, and total crack length (notch depth + main crack length measured by X-ray CT after interrupted tensile test), respectively. Before tensile testing, one side of the hydrogen-charged tensile specimens was lightly polished and etched to generate microstructure-based speckle patterns, which enable deformation mapping over a wide field of view using *ex-situ* DIC [34]. The OM images of the notch-root region, captured before and after deformation, were processed in VIC-2D to generate strain distribution maps. The 3D crack morphology was analyzed using X-ray CT. After interrupted tensile tests, a rectangular column (2 mm × 10 mm × 1 mm) containing the notch and cracks was cut from each single-edged tension specimen, then imaged in absorption-contrast mode during a 360° rotation (step size: 0.1°) with a 4 × objective at 100 kV acceleration voltage. The specimen was aligned as follows according to the X-ray CT system coordinates: ± X corresponds to the tensile axis, + Y corresponds to the macroscopic crack propagation direction, and ± Z corresponds to the thickness direction; all subsequent results refer to this coordinate system. The resulting dataset was segmented and meshed to render the 3D crack morphology using ORS Dragonfly Pro software.

3. Results

3.1. Microstructure characterization and thermal desorption analysis

Fig. 2 shows (a_1, b_1, c_1) the OM images, (a_2, b_2, c_2) the EBSD orientation maps overlaid with image quality maps, and (a_3, b_3, c_3) BSE images of the CG (a_1–a_3), MG (b_1–b_3), and FG (c_1–c_3) specimens. The average PAG sizes for the CG, MG, and FG specimens, measured from the OM images using the line intercept method, are approximately 266 μm, 70 μm, and 6.2 μm, respectively. The OM images and EBSD maps show that all specimens exhibit a hierarchical martensitic microstructure, characterized by blocks and packets within each PAG. Notably, the block and packet sizes decrease with the refinement of PAGs. This observation aligns with previous studies demonstrating that both the block and packet sizes exhibit a linear dependence on the PAG size in lath martensite [31,35–38]. The high-magnification BSE images in Fig. 2(a_3, b_3, c_3) reveal the internal lath structures and PAGBs (indicated by the white dashed lines). No precipitates or other phases are detected in each condition.

Fig. 3(a–c) show the hydrogen desorption profiles for the CG, MG, and FG specimens pre-charged under different conditions. The blue, red, and green curves represent hydrogen-charging current densities of 0.5, 1, and 1.5 A m^{-2}, respectively. The corresponding H_D values under these charging conditions are included in the figures. Fig. 3(d) summarizes the relationship between H_D and current density in the specimens with different PAG sizes. Under a given hydrogen-charging condition, the H_D increases with decreasing the PAG size, indicating a higher hydrogen absorption capacity. Moreover, as shown in Fig. 3(a–c), the main peak shifts to a higher temperature range with the refinement of PAG. For instance, at 1.5 A m^{-2}, the peak positions are 195 °C, 221 °C, and 230 °C for the CG, MG, and FG specimens, respectively. This shift indicates an increased contribution from strong trapping sites in refined microstructures. In lath martensitic steels, PAGBs generally act as stronger trapping sites than dislocations and block/sub-block boundaries [39–41]. The improved hydrogen absorption capacity from PAG refinement stems primarily from increased hydrogen-trapping sites,

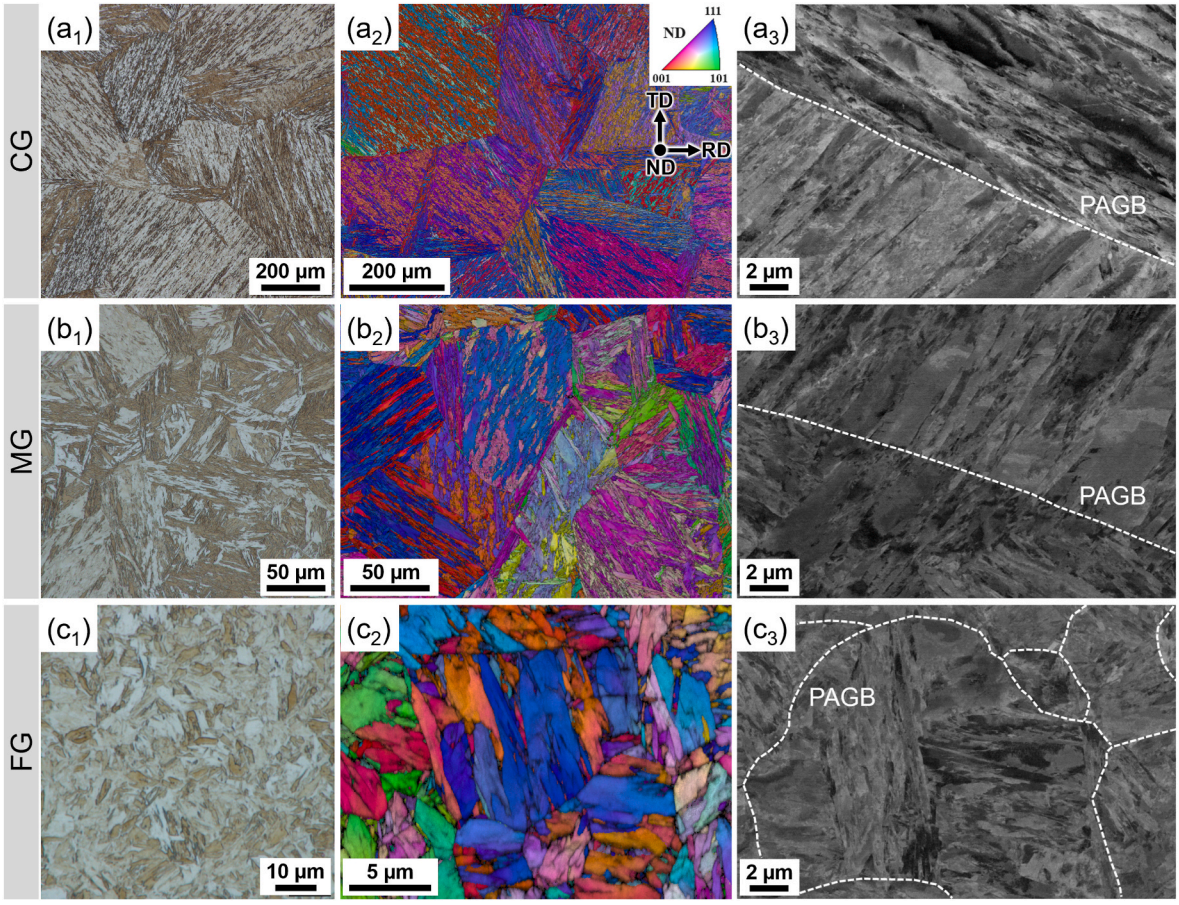

Fig. 2. The (a_1, b_1, c_1) OM images, (a_2, b_2, c_2) EBSD orientation maps over laid with image quality maps, and (a_3, b_3, c_3) BSE images of the (a_1–a_3) CG specimen, (b_1–b_3) MG specimen, and (c_1–c_3) FG specimen.

such as block/packet boundaries and PAGBs.

3.2. Mechanical properties and hydrogen embrittlement susceptibility

Fig. 4 presents the nominal stress–nominal strain curves of the (a) CG, (b) MG, and (c) FG specimens (unnotched) with different H_D. In the absence of hydrogen (black lines), both the tensile strength and ductility improve as the PAG size decreases. Specifically, the CG specimen exhibits a yield strength (σ_Y, 0.2 % proof stress) of 1103 MPa and an ultimate tensile strength (σ_{UTS}) of 1552 MPa. As the PAG size was refined to MG, the σ_Y and σ_{UTS} values increase to 1162 MPa and 1658 MPa, respectively. These values further increase to 1227 MPa and 1766 MPa in the FG specimen, demonstrating the expected improvement from PAG refinement. Meanwhile, the elongation to fracture also increases from 8.6 % (CG) to 13.9 % (FG), reflecting a synergistic improvement in strength and ductility with PAG refinement. In contrast, hydrogen presence causes significant degradation in both strength and ductility. The CG, MG, and FG specimens charged at 0.5 A m^{-2} (blue lines) exhibit very limited plasticity before fracture, with fracture strains of 1.1 %, 1.1 %, and 1.6 %, respectively. At a higher charging current density of 1.0 A m^{-2} (red lines), the CG specimen and MG specimen fracture within the apparent elastic regime, while the FG specimen retains some plasticity and fractures at high stress level of up to 1570 MPa. When charged at 1.5 A m^{-2} (green lines), all specimens exhibit a complete loss of plasticity, fracturing within the apparent elastic regime. These observations clearly illustrate that increasing H_D leads to a substantial reduction in both maximum tensile stress and ductility, clearly indicating premature failure caused by hydrogen embrittlement. Because all hydrogen-charged specimens fractured in or near the elastic regime (after only minimal plastic strain), plasticity loss fails to effectively differentiate their hydrogen embrittlement resistance. Therefore, this study adopts load-bearing capacity loss as the primary metric for hydrogen embrittlement, with ductility loss as a complementary measure.

Fig. 5(a) illustrates the correlation between maximum tensile stress and H_D in the unnotched specimens having different PAG sizes, demonstrating a clear hydrogen dependence of load-bearing capacity. The black, red, and green symbols denote the FG, MG, and CG specimens, respectively. The maximum tensile stress consistently decreases with increasing H_D across all specimens. It is notable that, under a similar H_D level, the specimen with finer PAGs shows higher maximum tensile stress, suggesting that PAG refinement can significantly enhance the load-bearing capacity. Due to differences in the σ_{UTS} of the uncharged specimens, the hydrogen embrittlement index (*HEI*)—defined as the ratio of maximum tensile stress reduction—was established to quantify the hydrogen embrittlement susceptibility, and expressed as [42]:

$$HEI = \frac{s_{max} - s_{max\_H}}{s_{max}} \tag{3}$$

where s_{max} and s_{max_H} denote the maximum tensile stress of the uncharged and hydrogen-charged specimens, respectively. Higher *HEI* values indicate lower resistance to hydrogen embrittlement. Fig. 5(b) shows the dependence of *HEI* on the H_D in the specimens with different PAG sizes. In all cases, the *HEI* increases with increasing the H_D. Within the investigated H_D range, the specimen with coarser PAG size exhibits more pronounced loss of load-bearing capacity. Moreover, the discrepancy in the *HEI* values between different PAG sizes becomes more pronounced at higher H_D levels, highlighting the superior hydrogen

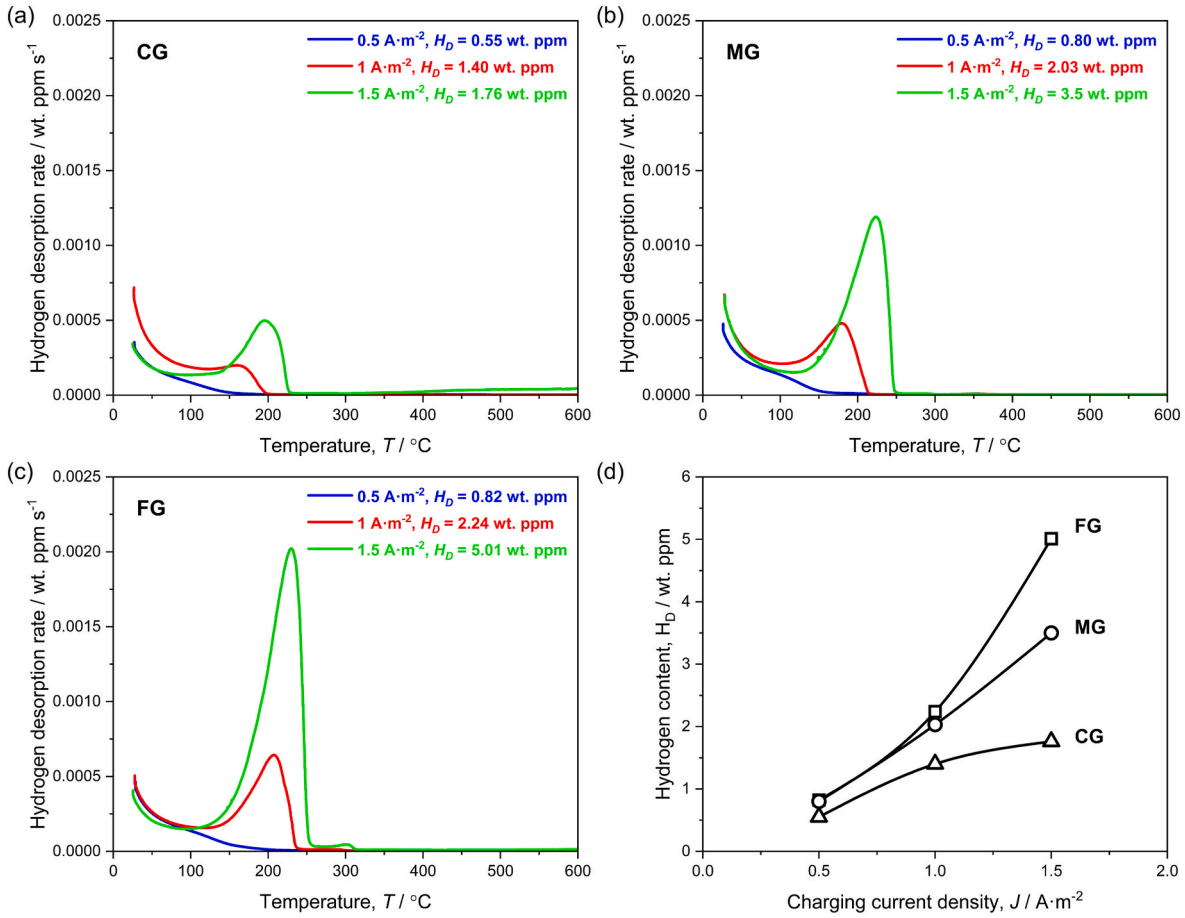

Fig. 3. Hydrogen desorption profiles for the hydrogen-charged specimens: (a) CG, (b) MG, and (c) FG, at current densities of 0.5 A m^{-2} (blue), 1 A m^{-2} (red), and 1.5 A m^{-2} (green); (d) H_D plotted against charging current density for the specimens with different PAG sizes. (For interpretation of the references to color in this figure legend, the reader is referred to the Web version of this article.)

embrittlement resistance in specimens with finer PAGs.

3.3. Fracture morphology

Fig. 6 presents the representative SEM images of the fracture surfaces of the CG and FG specimens, both without and with hydrogen pre-charging. As illustrated in Fig. 6(a_1–c_1), the uncharged specimens exhibit mixed fracture modes, characterized by coexisting cleavage facets and ductile dimples. In contrast, the hydrogen-charged specimens display quasi-cleavage and intergranular fracture features. The cleavage and quasi-cleavage fracture surfaces can be distinguished morphologically by their distinct features: river patterns on cleavage surfaces and serrated markings on quasi-cleavage surfaces [13]. White arrows in each figure indicate the locations of typical ductile dimples, cleavage facets, quasi-cleavage surfaces, and intergranular facets. For each PAG size, the intergranular fracture area fraction increases with rising H_D levels. Notably, the fracture surface morphology is also influenced by the PAG size. The average projected facet size was measured by the line intercept method on SEM images. The intergranular facet sizes were approximately 250 μm and 4.7 μm for the CG and FG specimens, respectively, closely matching their respective PAG sizes. In general, the quasi-cleavage and intergranular fracture facets were significantly larger in the CG specimens than in the FG specimens (see Fig. 6(a_2) and 6(c_2), or Fig. 6(a_3) and 6(c_3)). The fractographic analysis shows that the unit crack advance in lath martensite is also positively correlated with the PAG size, demonstrating PAG size-dependent crack propagation behavior.

3.4. Local plastic strain analysis

To examine how PAG size influences strain localization behavior and macroscopic 2D cracking behavior under similar H_D level, interrupted tensile tests integrated with *ex-situ* DIC were conducted on single-edge notched tension specimens. Fig. 7 exhibits (a_1, b_1, c_1) the OM images of the notch root regions showing the surface cracks (indicated by the yellow arrows) after the interrupted tensile tests and (a_2, b_2, c_2) the corresponding DIC strain distribution maps overlaid on the OM images of the CG, MG, and FG specimens with similar H_D. The average strain (e_{avg}) for each analyzed region is annotated in the figures. As shown in Fig. 7(a_1), a main crack and several sub-cracks are clearly observed in the CG specimen. The number of surface cracks increases as the PAG size decreases (see 7(b_1–c_1)). The specimen with finer PAG size shows higher densities of isolated small cracks (inset of Fig. 7(c_1)), which may be due to the increased density of PAGBs that can act as hydrogen traps and potential crack initiation sites. Notably, severe local plastic deformation is observed at the notch root of the FG specimen. The DIC strain distribution maps (Fig. 7(a_2–c_2)) demonstrate that all specimens deform in a highly heterogeneous manner. In the CG specimen, strain localization primarily occurs within blocks and along PAGBs, exhibiting a strong correlation with martensitic microstructure features, which is consistent with our previous study [34]. Under a similar H_D level, PAG refinement results in a shift from microstructure-related strain localization (Fig. 7(a_2)) to radial shear localization that penetrates multiple PAGs (Fig. 7(b_2 and c_2)). That is, the microstructure-related strain localization is mitigated with PAG refinement. Correlated OM and DIC analyses reveal that surface cracks predominantly nucleate at strain-localized regions,

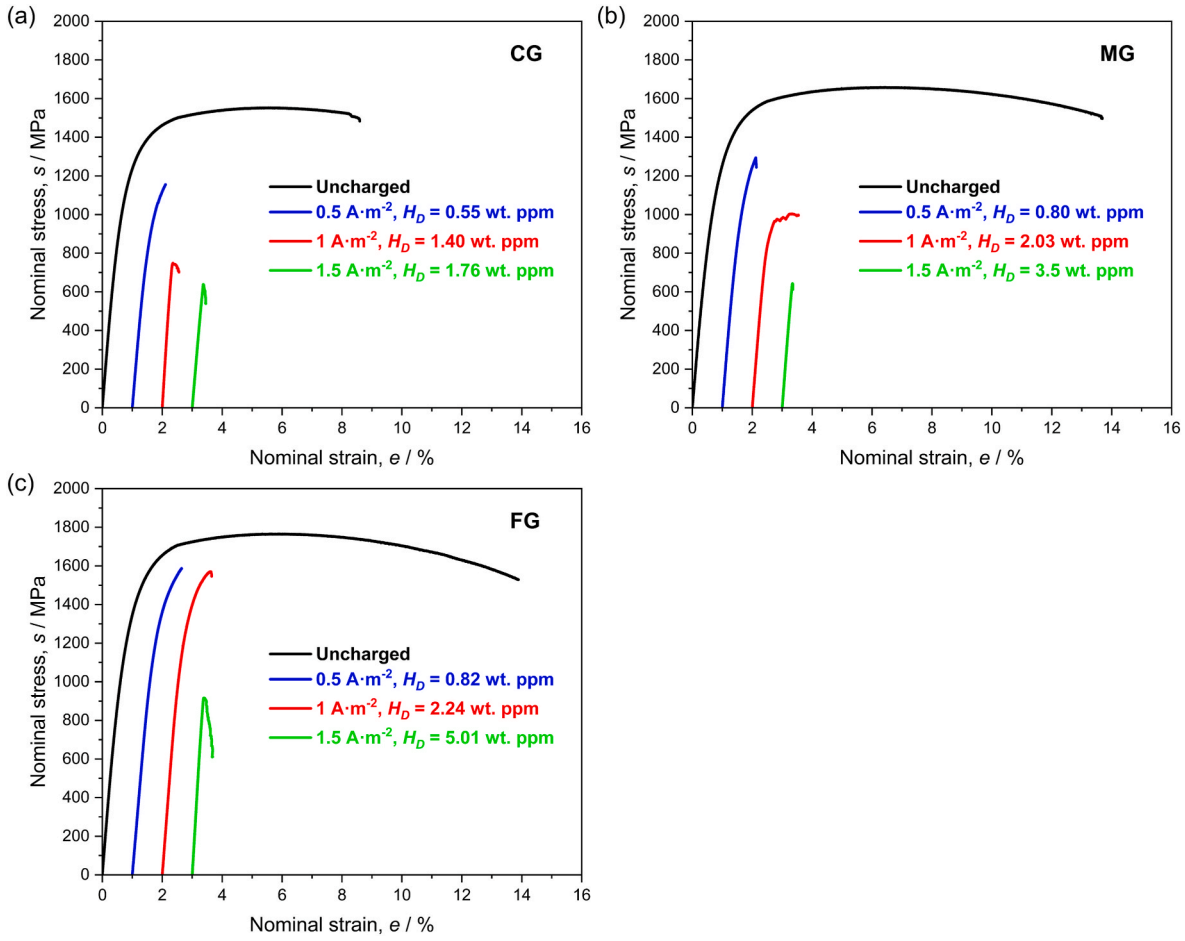

Fig. 4. Nominal stress–nominal strain curves of the (a) CG, (b) MG, and (c) FG specimens with different H_D.

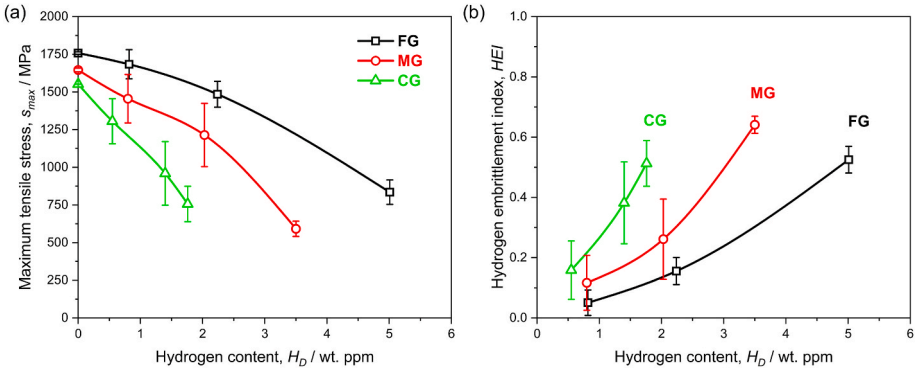

Fig. 5. (a) Maximum tensile stress as a function of H_D in specimens having different PAG sizes; (b) correlation between *HEI* and H_D in the specimens having different PAG sizes.

indicating that a threshold strain is required for cracking—and thus mitigating strain localization via PAG refinement improves hydrogen embrittlement resistance.

3.5. Macroscopic 3D analysis of crack propagation

Fig. 8 presents the macroscopic 3D crack morphologies obtained via X-ray CT after interrupted tensile tests on specimens with different PAG sizes: (a_1, a_2) CG specimen (H_D = 1.76 wt ppm; voxel size: 0.86^3 μm^3), (b_1, b_2) MG specimen (H_D = 2.03 wt ppm; voxel size: 0.86^3 μm^3), and (c_1, c_2) FG specimen (H_D = 2.24 wt ppm; voxel size: 1.26^3 μm^3). The reconstructed absorption-contrast images were processed using the U-Net model implemented in ORS Dragonfly Pro to segment the crack regions. Post-segmentation, the crack regions were meshed, and the thickness of each crack component was calculated as the diameter of a hypothetical sphere that fits within each boundary point. In Fig. 8(a_2, b_2, c_2), the crack thickness is depicted through color variations corresponding to the provided color scale. Generally, the crack thickness diminishes as it approaches the crack tip. The 3D crack morphology clearly reveals that the CG specimen predominantly exhibits intergranular fracture features. The MG specimen displays intergranular fracture features near the notch root and transgranular fracture features near the

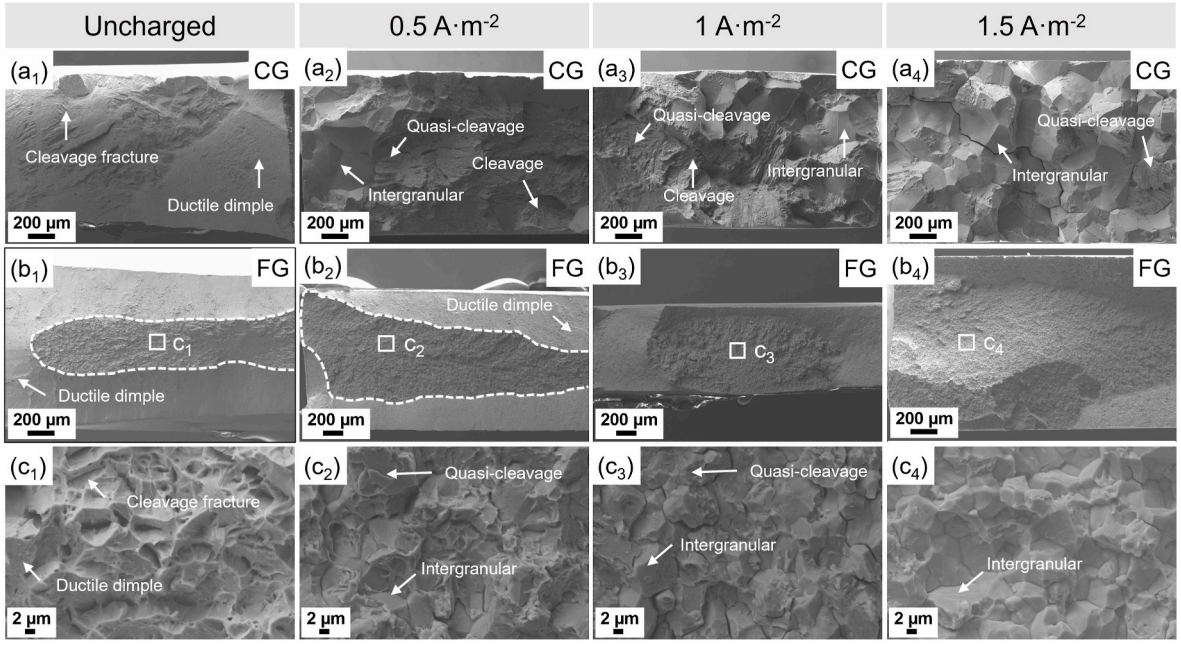

Fig. 6. SEM images of the fracture surfaces after SSRT: (a_1–a_4) CG specimens and (b_1–b_4) FG specimens, both without and with hydrogen pre-charging. (c_1–c_4) Magnified views of the areas marked in (b_1–b_4).

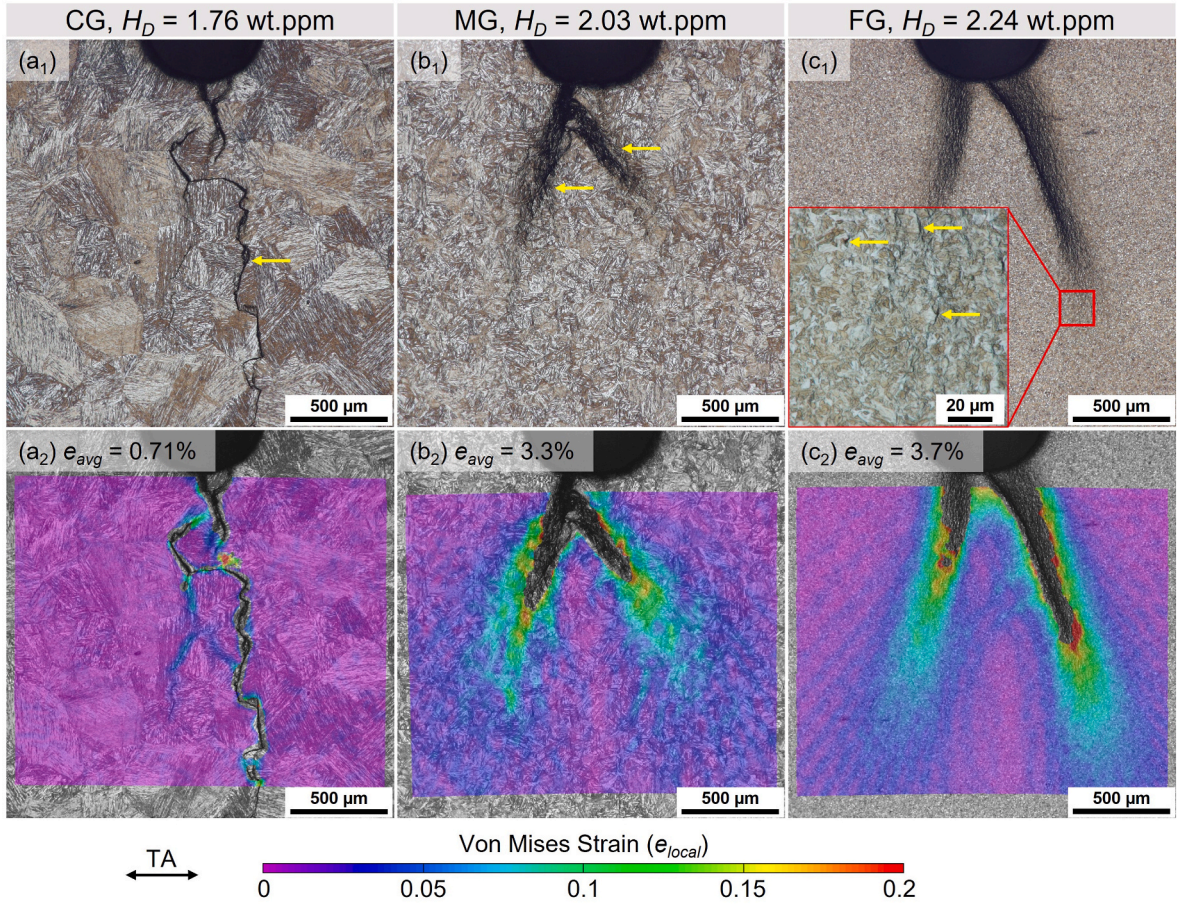

Fig. 7. (a_1, b_1, c_1) OM images of the notch root regions showing the surface cracks after the interrupted tensile tests and (a_2, b_2, c_2) corresponding DIC plastic strain distribution maps overlaid on the OM images of the CG, MG, and FG specimens with similar H_D. TA: tensile axis.

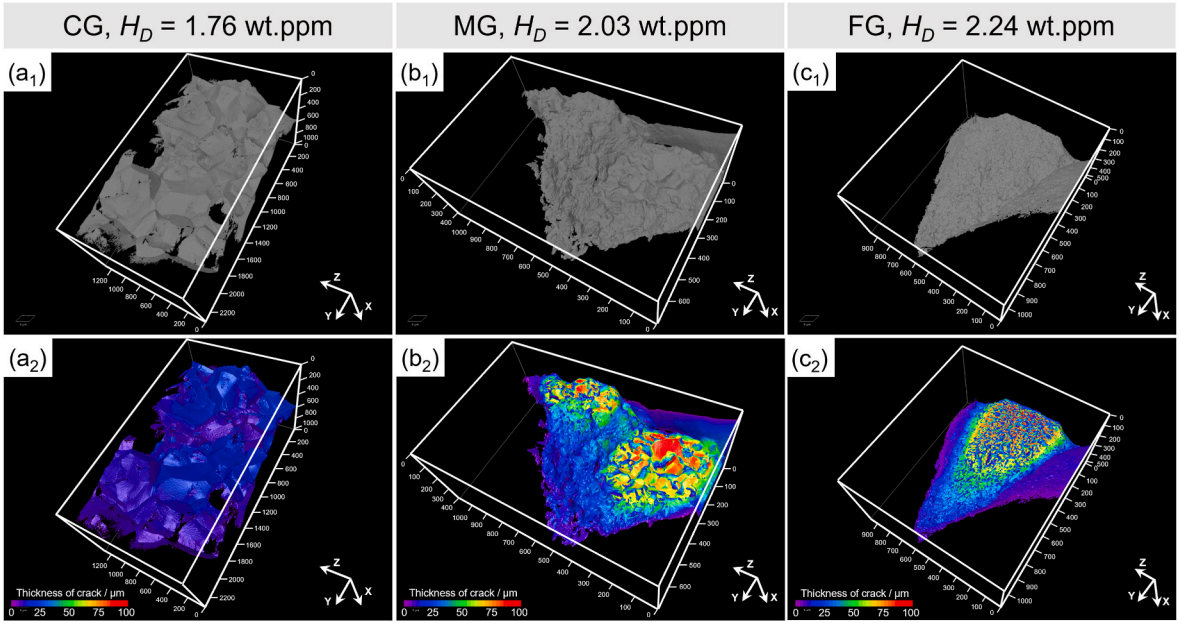

Fig. 8. Macroscopic 3D crack morphologies reconstructed by X-ray CT for the (a_1, a_2) CG specimen, (b_1, b_2) MG specimen, and (c_1, c_2) FG specimen with similar H_D.

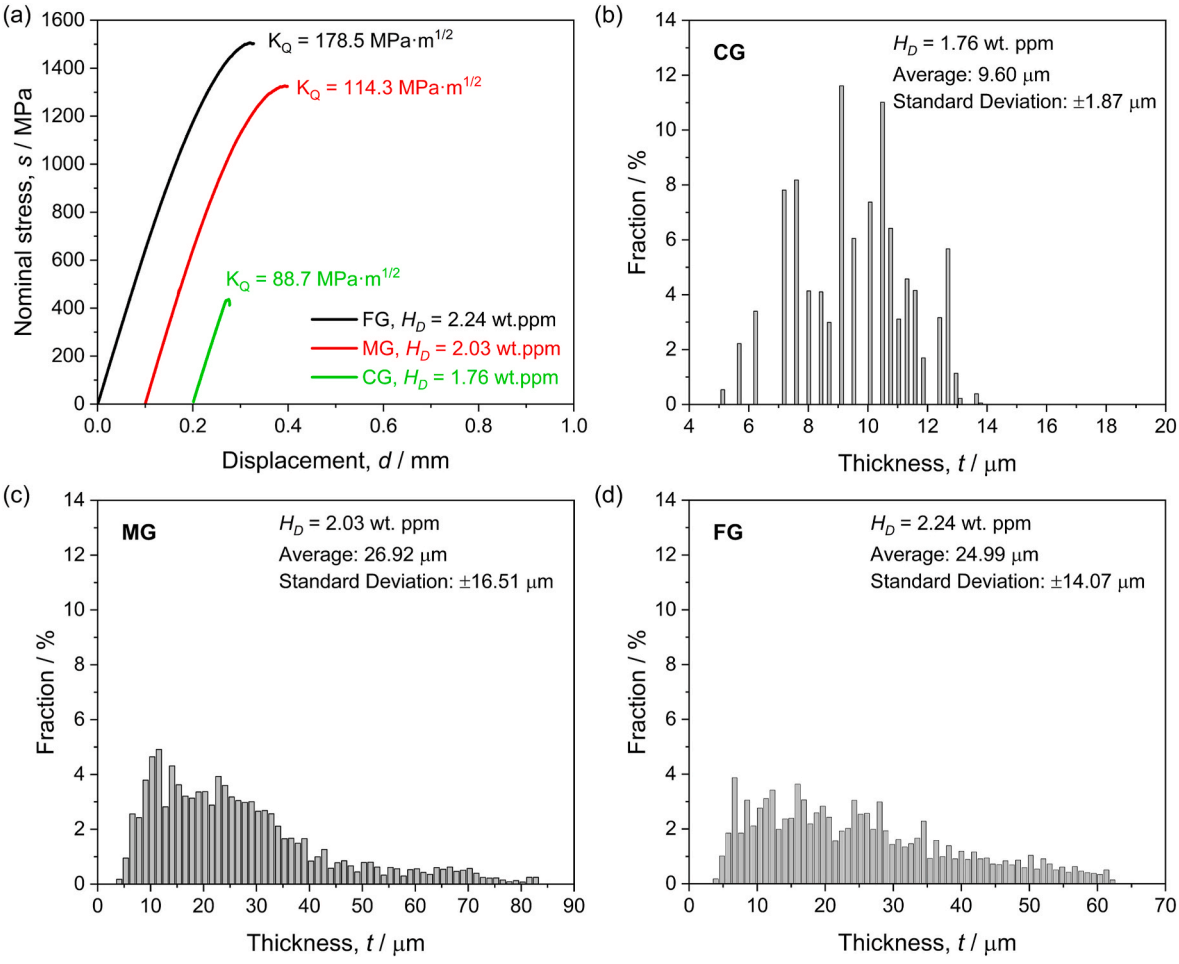

Fig. 9. (a) Nominal stress–displacement curves for the single-edge notched tension specimens with similar H_D, obtained from interrupted tensile tests; crack thickness profiles near the crack tip in the (b) CG specimen, (c) MG specimen, and (d) FG specimen.

crack tip. Although the limited spatial resolution (voxel size: 1.26^3 μm^3) relative to the small PAG size (6.2 μm) in the FG specimen complicates the identification of fracture features from the 3D crack morphology, frequent crack deflections are still discernible. Notably, hydrogen-related intergranular cracks propagate with much smaller crack-opening displacements (crack thickness) in the CG specimen. PAG refinement was found to exert a dual effect on crack deflection: the amplitude decreases while the frequency increases. These observations from the 3D crack morphologies, in conjunction with the 2D fracture surface analyses presented in Fig. 6, indicate a strong dependence of hydrogen-related crack propagation behavior on PAG size.

Then we quantitatively analyzed the crack thickness near the crack tip, using identical analyzed volumes of 400 × 600 × 300 μm^3 for all specimens. Fig. 9(a) shows the nominal stress–displacement curves for the notched CG, MG, and FG specimens with similar H_D, obtained from interrupted tensile tests. The apparent fracture toughness K_Q at the onset of cracking was determined to be 88.7 MPa m$^{1/2}$, 114.3 MPa m$^{1/2}$, and 178.5 MPa m$^{1/2}$ for the CG, MG, and FG specimens, respectively. Fig. 9 (b–d) presents the crack thickness profiles for the CG, MG, and FG specimens. The average crack thickness values are 9.6 ± 1.87 μm, 26.9 ± 16.51 μm, and 25 ± 14.07 μm for the CG, MG, and FG specimens, respectively. The average crack tip thickness of the CG specimen is significantly smaller than that of the FG and MG specimens. These findings suggest that in the CG specimen, hydrogen-related intergranular cracks propagate at substantially reduced crack-opening displacement. This behavior is attributed to elevated local hydrogen concentrations at PAGBs, which reduce the cohesive energy of PAGBs and consequently lowers the stress level required for intergranular decohesion. However, further refinement from MG to FG does not lead to an increase in the average crack thickness, suggesting comparable local plastic deformation near the crack front.

4. Discussion

4.1. Correlation between apparent fracture toughness, crack surface energy, and plastic work

From an energy perspective, fracture occurs when the strain energy release rate reaches or exceeds the critical energy (fracture energy, w_f) required to create new fracture surfaces and to overcome other dissipative processes (mainly plastic work, γ_p). Although plastic work generally dominates over crack surface energy (γ_s), its precise contribution to macroscopic fracture toughness is difficult to quantify due to heterogeneous local strain distributions (as shown in Fig. 7) and the unknown local stress state. Therefore, the contribution of plastic work to fracture energy was estimated using a semi-quantitative approach with

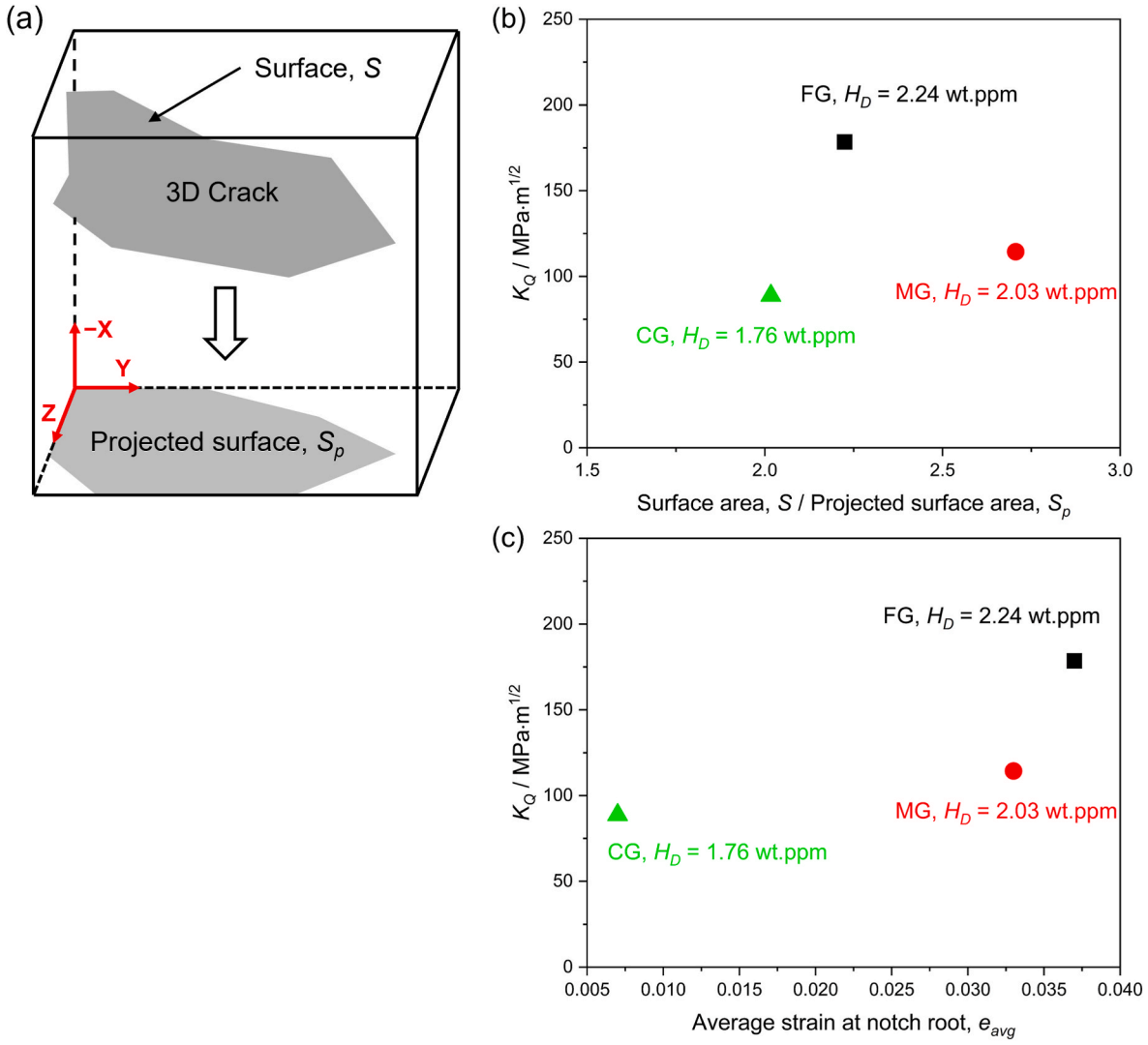

Fig. 10. (a) Schematic illustration of the actual crack surface area (S) and its projected area (Sp) on the YZ plane; (b) correlation between the K_Q and the S/Sp ratio in the CG, MG, and FG specimens with similar H_D; (c) correlation between the K_Q and the e_{avg} at notch root area in the CG, MG, and FG specimens with similar H_D.

DIC analysis. Fracture energy is also influenced by crack meandering and branching, which increase the crack surface area. For materials exhibiting such features, the fracture energy can be formulated as [33]:

$$w_f = \gamma_s \frac{S}{S_p} + \gamma_p \tag{4}$$

where S is the actual crack surface area and Sp is its projection onto the macroscopic crack plane, as schematically illustrated in Fig. 10(a). The ratio S/Sp quantifies the extent of crack meandering and branching. Fig. 10(b) shows the correlation between K_Q and the S/Sp ratio for the CG, MG, and FG specimens with similar H_D. While larger S/Sp values generally correlate with greater fracture energy consumption, the trend with PAG refinement is non-monotonic. Specifically, the FG specimen exhibits the highest K_Q, with its S/Sp value being second only to that of the MG specimen, whereas the CG specimen shows the lowest S/Sp value and significantly lower K_Q than the FG and MG specimens. This behavior reflects two competing microstructure-driven effects: (i) PAG refinement increases the frequency of crack branching and meandering, raising the crack surface area and energy consumption; (ii) PAG refinement reduces individual facet size, lowering surface area created per deflection. The observed peak in S/Sp at intermediate PAG size (MG in this study) therefore results from the balance of these competing effects. The non-monotonic trend highlights the role of plastic work, as illustrated in Fig. 10(c). DIC analysis at the notch root (Fig. 7) shows that the average plastic strain increases as PAG size decreases, indicating a greater plastic-work dissipation—defined as the integral of stress beyond the elastic limit with respect to strain. This observation is consistent with Fig. 9(a), where both fracture stress and plastic strain increase as the PAG size decreases. In short, while increased crack meandering and branching (higher S/Sp value) supplements fracture resistance within a specific PAG size range, the primary gain in K_Q with PAG refinement is driven by the microstructure's enhanced capacity to accommodate plastic deformation.

4.2. Role of PAG refinement on hydrogen-related fracture

Figs. 4 and 5 demonstrate that PAG refinement, despite being associated with the increased hydrogen absorption capacity under a given hydrogen-charging condition, effectively reduces the hydrogen embrittlement susceptibility in as-quenched martensitic steel. The observed dependence of total hydrogen content (C_{TOT}) on PAG size can be decomposed into contributions from the PAGBs (C_{GB}) and the matrix (C_M), as expressed by the following equation [42]:

$$C_{TOT} = C_{GB} + C_M = a_{GB} S_{GB} + C_M \tag{5}$$

where a_{GB} represents the hydrogen content per unit area of PAGBs and S_{GB} denotes the total PAGB area per unit mass, which is related to the mean linear intercept length (L, unit: μm) of PAGs and the material density ρ (unit: g/cm^3) through $S_{GB} = 2/\rho L$. The S_{GB} increases with decreasing the PAG size. Studies have shown that as the PAG size is refined into the fine range, the number of martensite variants per PAG decreases, and the morphologies of packets and blocks become more equiaxed [37,38], potentially altering the crystallographic features of PAGBs. However, in this discussion, we do not take into account the potential changes in crystallographic features of PAGBs depending on PAG size. Both Takaki et al. [43] and Kennett et al. [44] showed that the dislocation density in as-quenched martensitic steels exhibits only a slight increase with decreasing PAG size, as measured by XRD. Similarly, Morito et al. [45] observed nearly identical dislocation densities in Fe-2Mn-0.2C lath martensite over a wide PAG size range (6 μm and 346 μm) using TEM. These findings suggest that the variations in dislocation density—and thus their contribution to C_M—are statistically insignificant within the current PAG size range (6 μm–266 μm). Therefore, the increased hydrogen absorption capacity observed with PAG refinement (Fig. 3) can primarily be attributed to the larger block/packet and PAG boundary areas. Since the differences in C_{TOT} among specimens with varying PAG sizes are much smaller than the differences in boundary area, it is reasonable to deduce that the a_{GB} decreases significantly with PAG refinement. Momotani et al. [46,47] investigated hydrogen accumulation behavior in lath martensite during deformation using the hydrogen micro-print technique. Their results indicated that hydrogen preferentially accumulates at PAGBs during deformation, with elevated hydrogen concentrations at these boundaries promoting intergranular cracking. Therefore, PAG refinement reduces local hydrogen accumulation at PAGBs, resulting in a decreased frequency of hydrogen-induced intergranular fracture under a similar H_D level.

The hydrogen-induced mechanical degradation cannot be attributed solely to the PAG size-dependent hydrogen concentration at the PAGBs. Shibata et al. [14] investigated hydrogen-related fracture in low-carbon martensitic steel and demonstrated that quasi-cleavage cracks invariably initiated at peak plastic strain locations, despite variations in the local hydrogen content, plastic strain, and principal stress at quasi-cleavage initiation sites with the stress concentration factor, quasi-cleavage cracks always initiated at peak plastic strain locations. Complementary to this, our earlier work [34] revealed that strain localization in martensitic steel occurs predominantly within martensite blocks and along PAGBs, exhibiting a strong correlation with martensitic microstructure features, regardless of hydrogen presence. The results also showed that hydrogen lowers the threshold local strain required for quasi-cleavage crack initiation and strain localization plays a role in hydrogen-induced intergranular cracking, linking both failure modes to localized plastic deformation. The DIC results in Fig. 7 show that PAG refinement results in a shift from microstructure-related strain localization (CG specimen) to radial shear localization that penetrates multiple PAGs (FG specimen) under a similar H_D level. We propose that the microstructure-related strain localization is mitigated with PAG refinement, reducing the local accumulation of hydrogen at PAGBs. Simultaneously, under a similar global strain level, the lower local stress/strain level makes it more difficult to initiate cracking.

The fracture surfaces in Fig. 6 reveal how hierarchical martensitic microstructures influence the crack paths and deflections, which ultimately govern the fracture behavior. Therefore, crack morphology is another important factor that must be taken into consideration while assessing the resistance to hydrogen-related fracture. Hydrogen-related intergranular fracture predominantly occurs along PAGBs [4,17,18,48]. When the PAGs are small, the hydrogen-related intergranular cracks frequently deflect, delaying their propagation along PAGBs. In contrast, hydrogen-related quasi-cleavage fracture propagates parallel to {011} planes within martensite laths [13,14,49]. The crystallographic misorientations of block and packet boundaries are basically high, requiring more energy for a transgranular crack to cross them. Indeed, Morris et al. [8,50,51] and Shibata et al. [52] have proposed that in martensitic steels, variant boundaries—usually correspond to block and packet boundaries—with large misorientation between {001} cleavage planes act as barriers, effectively retarding cleavage fracture. Similarly, Cho et al. [25] demonstrated that high-angle martensitic boundaries cause significant deflections of hydrogen-related quasi-cleavage cracks in martensitic steel. These high-angle martensitic boundaries act as obstacles to quasi-cleavage crack propagation, which partially explains why lath martensitic steels with smaller PAGs (and thus smaller martensite blocks and packets) exhibit greater resistance to hydrogen embrittlement.

As discussed in Section 4.1, the fracture energy increases when cracks meander or branch, since both processes increase the crack surface area. The extent of crack meandering and branching can be quantitatively evaluated by the 3D X-ray CT analysis, as illustrated in Fig. 10. Shibata et al. [53] reported that, in martensitic steel with varying H_D levels, the J-integral value increased monotonically with the ratio of actual-to-projected crack surface area (S/Sp), suggesting that the fracture energy was improved by increased crack meandering and branching. However, our current study reveals that the K_Q does not exhibit a

monotonic increase with the *S/Sp* ratio. The *S/Sp* ratio depends on the frequency of crack branching/meandering as well as each crack facet size. The PAG refinement can increase the frequency of crack deflection but decrease the crack facet size, as shown in Figs. 6 and 8. Consequently, these combined effects of PAG refinement would lead to a peak *S/Sp* value at a medium PAG size range. Overall, the *S/Sp* parameter can serve as an effective supplement for evaluating hydrogen-related fracture resistance within a specific PAG size range, though the plastic work remains the dominant factor.

5. Conclusions

This study presents a multimodal, quantitative assessment of PAG size effects on hydrogen embrittlement behavior in high-strength martensitic steel. The hydrogen embrittlement susceptibility was evaluated via SSRT, while the PAG size effects on strain localization and macroscopic 3D crack propagation were investigated through interrupted tensile tests integrated with *ex-situ* DIC and X-ray CT. The main findings are summarized as follows.

(1) Under a similar H_D level, the specimens with finer PAGs exhibited higher load-bearing capacity and lower *HEI*, indicating that PAG refinement can effectively enhance the hydrogen embrittlement resistance of martensitic steel.
(2) The susceptibility to hydrogen embrittlement originated from plastic deformation associated with the microstructural characteristics of lath martensite. Under a similar H_D level, PAG refinement mitigated the microstructure-related strain localization, thereby enhancing the hydrogen embrittlement resistance.
(3) PAG refinement increased the apparent fracture toughness under a similar H_D level. This improvement arises from two synergistic mechanisms: (i) increased plastic-work dissipation, which is the primary contributor to the toughness gain, and (ii) increased crack meandering/branching (quantified by *S/Sp* ratio), which adds fracture-surface area but depends non-monotonically on PAG size—peaking at intermediate PAG size and declining with further refinement.
(4) The enhanced resistance to hydrogen embrittlement associated with PAG refinement could be attributed to several factors: reduced strain localization, lower local hydrogen concentration per unit area of PAGBs, increased deflection of intergranular cracks, and a higher density of high-angle boundaries that impede quasi-cleavage cracks—all facilitated by PAG refinement. These findings establish PAG refinement as an effective strategy for developing hydrogen-resistant high-strength martensitic steels despite the processing complexity may limit large-scale production. We expect it to be adopted primarily for critical hydrogen infrastructure components where failure consequences outweigh manufacturing complexity.

CRediT authorship contribution statement

Xiaodong Lan: Writing – review & editing, Writing – original draft, Visualization, Software, Methodology, Investigation, Formal analysis, Data curation, Conceptualization. **Kazuho Okada:** Writing – review & editing, Validation, Funding acquisition. **Ivan Gutierrez-Urrutia:** Writing – review & editing, Validation. **Akinobu Shibata:** Writing – review & editing, Visualization, Validation, Supervision, Software, Resources, Project administration, Funding acquisition, Conceptualization.

Declaration of competing interest

The authors declare that they have no known competing financial interests or personal relationships that could have appeared to influence the work reported in this paper.

Acknowledgements

This work was financially supported by JSPS KAKENHI (Grant Numbers JP22K18910, JP23H01717, JP23K13541, and JP24K01221) and MEXT Program: Data Creation and Utilization Type Material Research and Development Project Grant Number JPMXP1122684766.

Data availability

Data will be made available on request.

References

[1] D. Raabe, C.C. Tasan, E.A. Olivetti, Strategies for improving the sustainability of structural metals, Nature 575 (2019) 64–74, https://doi.org/10.1038/s41586-019-1702-5.
[2] B. Sun, W. Lu, B. Gault, R. Ding, S.K. Makineni, D. Wan, C.-H. Wu, H. Chen, D. Ponge, D. Raabe, Chemical heterogeneity enhances hydrogen resistance in high-strength steels, Nat. Mater. 20 (2021) 1629–1634, https://doi.org/10.1038/s41563-021-01050-y.
[3] I.M. Robertson, P. Sofronis, A. Nagao, M.L. Martin, S. Wang, D.W. Gross, K. E. Nygren, Hydrogen embrittlement understood, Metall. Mater. Trans. 46 (2015) 2323–2341, https://doi.org/10.1007/s11661-015-2836-1.
[4] A. Shibata, T. Murata, H. Takahashi, T. Matsuoka, N. Tsuji, Characterization of hydrogen-related fracture behavior in As-Quenched low-carbon martensitic steel and tempered medium-carbon martensitic steel, Metall Mater Trans A Phys Metall Mater Sci 46 (2015) 5685–5696, https://doi.org/10.1007/s11661-015-3176-x.
[5] A. Shibata, G. Miyamoto, S. Morito, A. Nakamura, T. Moronaga, H. Kitano, I. Gutierrez-Urrutia, T. Hara, K. Tsuzaki, Substructure and crystallography of lath martensite in as-quenched interstitial-free steel and low-carbon steel, Acta Mater. 246 (2023) 118675, https://doi.org/10.1016/j.actamat.2023.118675.
[6] S. Morito, H. Tanaka, R. Konishi, T. Furuhara, T. Maki, The morphology and crystallography of lath martensite in Fe-C alloys, Acta Mater. 51 (2003) 1789–1799, https://doi.org/10.1016/S1359-6454(02)00577-3.
[7] S. Morito, X. Huang, T. Furuhara, T. Maki, N. Hansen, The morphology and crystallography of lath martensite in alloy steels, Acta Mater. 54 (2006) 5323–5331, https://doi.org/10.1016/j.actamat.2006.07.009.
[8] C.C. Kinney, K.R. Pytlewski, A.G. Khachaturyan, J.W. Morris, The microstructure of lath martensite in quenched 9Ni steel, Acta Mater. 69 (2014) 372–385, https://doi.org/10.1016/j.actamat.2014.01.058.
[9] T. Ohmura, K. Tsuzaki, S. Matsuoka, Nanohardness measurement of high-purity Fe–C martensite, Scr. Mater. 45 (2001) 889–894, https://doi.org/10.1016/S1359-6462(01)01121-6.
[10] Y.-S. Chen, H. Lu, J. Liang, A. Rosenthal, H. Liu, G. Sneddon, I. McCarroll, Z. Zhao, W. Li, A. Guo, J.M. Cairney, Observation of hydrogen trapping at dislocations, grain boundaries, and precipitates, Science 367 (1979) 171–175, https://doi.org/10.1126/science.aaz0122, 2020.
[11] A. Pundt, R. Kirchheim, Hydrogen in metals: microstructural aspects, Annu. Rev. Mater. Res. 36 (2006) 555–608, https://doi.org/10.1146/annurev.matsci.36.090804.094451.
[12] B. Sun, W. Krieger, M. Rohwerder, D. Ponge, D. Raabe, Dependence of hydrogen embrittlement mechanisms on microstructure-driven hydrogen distribution in medium Mn steels, Acta Mater. 183 (2020) 313–328, https://doi.org/10.1016/j.actamat.2019.11.029.
[13] A. Shibata, Y. Momotani, T. Murata, T. Matsuoka, M. Tsuboi, N. Tsuji, Microstructural and crystallographic features of hydrogen-related fracture in lath martensitic steels, Mater. Sci. Technol. 33 (2017) 1524–1532, https://doi.org/10.1080/02670836.2017.1312210.
[14] A. Shibata, T. Yonemura, Y. Momotani, M. Park, S. Takagi, Y. Madi, J. Besson, N. Tsuji, Effects of local stress, strain, and hydrogen content on hydrogen-related fracture behavior in low-carbon martensitic steel, Acta Mater. 210 (2021) 116828, https://doi.org/10.1016/j.actamat.2021.116828.
[15] G. Wang, Y. Yan, J. Li, J. Huang, Y. Su, L. Qiao, Hydrogen embrittlement assessment of ultra-high strength steel 30CrMnSiNi2, Corros. Sci. 77 (2013) 273–280, https://doi.org/10.1016/j.corsci.2013.08.013.
[16] A. Shibata, Y. Madi, K. Okada, N. Tsuji, J. Besson, Mechanical and microstructural analysis on hydrogen-related fracture in a martensitic steel, Int. J. Hydrogen Energy 44 (2019) 29034–29046, https://doi.org/10.1016/j.ijhydene.2019.09.097.
[17] A. Shibata, I. Gutierrez-Urrutia, A. Nakamura, K. Okada, G. Miyamoto, Y. Madi, J. Besson, T. Hara, K. Tsuzaki, Three-dimensional propagation behavior of hydrogen-related intergranular cracks in high-strength martensitic steel, Int. J. Hydrogen Energy 48 (2023) 34565–34574, https://doi.org/10.1016/j.ijhydene.2023.05.211.
[18] M. Wang, E. Akiyama, K. Tsuzaki, Hydrogen degradation of a boron-bearing steel with 1050 and 1300 MPa strength levels, Scr. Mater. 52 (2005) 403–408, https://doi.org/10.1016/j.scriptamat.2004.10.023.
[19] Y. Hagihara, T. Shobu, N. Hisamori, H. Suzuki, K. Takai, K. Hirai, Delayed fracture using CSRT and hydrogen trapping characteristics of V-bearing high-strength steel, ISIJ Int. 52 (2012) 298–306, https://doi.org/10.2355/isijinternational.52.298.
[20] H.K.D.H. Bhadeshia, Prevention of hydrogen embrittlement in steels, ISIJ Int. 56 (2016) 24–36, https://doi.org/10.2355/isijinternational.ISIJINT-2015-430.

[21] T. Depover, K. Verbeken, The effect of TiC on the hydrogen induced ductility loss and trapping behavior of Fe-C-Ti alloys, Corros. Sci. 112 (2016) 308–326, https://doi.org/10.1016/j.corsci.2016.07.013.
[22] K. Okada, A. Shibata, T. Sasaki, H. Matsumiya, K. Hono, N. Tsuji, Improvement of resistance against hydrogen embrittlement by controlling carbon segregation at prior austenite grain boundary in 3Mn-0.2C martensitic steels, Scr. Mater. 224 (2023) 115043, https://doi.org/10.1016/j.scriptamat.2022.115043.
[23] K. Okada, A. Shibata, Y. Kimura, M. Yamaguchi, K. Ebihara, N. Tsuji, Effect of carbon segregation at prior austenite grain boundary on hydrogen-related crack propagation behavior in 3Mn-0.2C martensitic steels, Acta Mater. 280 (2024) 120288, https://doi.org/10.1016/j.actamat.2024.120288.
[24] M.J. Gomes da Silva, J.L. Cardoso, D.S. Carvalho, L.P.M. Santos, L.F.G. Herculano, H.F. Gomes de Abreu, J.M. Pardal, The effect of prior austenite grain size on hydrogen embrittlement of Co-containing 18Ni 300 maraging steel, Int. J. Hydrogen Energy 44 (2019) 18606–18615, https://doi.org/10.1016/j.ijhydene.2019.05.074.
[25] L. Cho, P.E. Bradley, D.S. Lauria, M.L. Martin, M.J. Connolly, J.T. Benzing, E.J. Seo, K.O. Findley, J.G. Speer, A.J. Slifka, Characteristics and mechanisms of hydrogen-induced quasi-cleavage fracture of lath martensitic steel, Acta Mater. 206 (2021) 116635, https://doi.org/10.1016/j.actamat.2021.116635.
[26] L. Cho, P.E. Bradley, D.S. Lauria, M.J. Connolly, E.J. Seo, K.O. Findley, J.G. Speer, L. Golem, A.J. Slifka, Effects of hydrogen pressure and prior austenite grain size on the hydrogen embrittlement characteristics of a press-hardened martensitic steel, Int. J. Hydrogen Energy 46 (2021) 24425–24439, https://doi.org/10.1016/j.ijhydene.2021.05.005.
[27] T. Chen, Y. Ogawa, M. Koyama, Growth path and morphology of hydrogen-related cracks in grain-refined tempered martensitic steel produced by cyclic thermal treatment, Int. J. Hydrogen Energy 136 (2025) 731–741, https://doi.org/10.1016/j.ijhydene.2024.05.327.
[28] A. Shibata, I. Gutierrez-Urrutia, A. Nakamura, G. Miyamoto, Y. Madi, J. Besson, T. Hara, K. Tsuzaki, Multi-scale three-dimensional analysis on local arrestability of intergranular crack in high-strength martensitic steel, Acta Mater. 234 (2022) 118053, https://doi.org/10.1016/j.actamat.2022.118053.
[29] A. Shibata, I. Gutierrez-Urrutia, A. Nakamura, T. Moronaga, K. Okada, Y. Madi, J. Besson, T. Hara, Local crack arrestability and deformation microstructure evolution of hydrogen-related fracture in martensitic steel, Corros. Sci. 233 (2024) 112092, https://doi.org/10.1016/j.corsci.2024.112092.
[30] X. Lan, K. Okada, R. Ueji, A. Shibata, Improving hydrogen embrittlement resistance in high-strength martensitic steels via thermomechanical processing, Scr. Mater. 264 (2025) 116711, https://doi.org/10.1016/j.scriptamat.2025.116711.
[31] T. Furuhara, K. Kikumoto, H. Saito, T. Sekine, T. Ogawa, S. Morito, T. Maki, Phase transformation from fine-grained austenite, ISIJ Int. 48 (2008) 1038–1045, https://doi.org/10.2355/isijinternational.48.1038.
[32] A. Shibata, S. Daido, D. Terada, N. Tsuji, Microstructures of pearlite and martensite transformed from ultrafine-grained austenite fabricated through cyclic heat treatment in medium carbon steels, Mater. Trans. 54 (2013) 1570–1574, https://doi.org/10.2320/matertrans.MH201312.
[33] T.L. Anderson, Fracture Mechanics: Fundamentals and Applications, fourth ed., CRC Press, 2017 https://doi.org/10.1201/9781315370293.
[34] X. Lan, K. Okada, I. Gutierrrez-Urrutia, A. Shibata, Quantitative analysis of local plasticity accompanying hydrogen-related fracture in low-carbon martensitic steel, Int. J. Hydrogen Energy 50 (2024) 333–341, https://doi.org/10.1016/j.ijhydene.2023.10.273.
[35] E.I. Galindo-Nava, P.E.J. Rivera-Díaz-Del-Castillo, A model for the microstructure behaviour and strength evolution in lath martensite, Acta Mater. 98 (2015) 81–93, https://doi.org/10.1016/j.actamat.2015.07.018.
[36] C. Wang, M. Wang, J. Shi, W. Hui, H. Dong, Effect of microstructural refinement on the toughness of low carbon martensitic steel, Scr. Mater. 58 (2008) 492–495, https://doi.org/10.1016/j.scriptamat.2007.10.053.
[37] J. Hidalgo, M.J. Santofimia, Effect of prior austenite grain size refinement by thermal cycling on the microstructural features of As-Quenched lath martensite, Metall Mater Trans A Phys Metall Mater Sci 47 (2016) 5288–5301, https://doi.org/10.1007/s11661-016-3525-4.
[38] S. Morito, H. Saito, T. Ogawa, T. Furuhara, T. Maki, Effect of austenite grain size on the morphology and crystallography of lath martensite in low carbon steels, ISIJ Int. 45 (2005) 91–94, https://doi.org/10.2355/isijinternational.45.91.
[39] Y.S. Chen, C. Huang, P.Y. Liu, H.W. Yen, R. Niu, P. Burr, K.L. Moore, E. Martínez-Pañeda, A. Atrens, J.M. Cairney, Hydrogen trapping and embrittlement in metals – a review, Int. J. Hydrogen Energy (2024), https://doi.org/10.1016/j.ijhydene.2024.04.076.
[40] N. Parvathavarthini, S. Saroja, R.K. Dayal, H.S. Khatak, Studies on hydrogen permeability of 2.25% Cr–1% Mo ferritic steel: correlation with microstructure, J. Nucl. Mater. 288 (2001) 187–196, https://doi.org/10.1016/S0022-3115(00)00706-6.
[41] K. Matsubara, S. Takagi, F.-S. Meng, S. Ogata, N. Ishikawa, Atomic-scale modelling of boundaries characterized lath martensite microstructure for hydrogen-induced crack initiation: a machine learning interatomic potentials study. Proceedings of International Symposia on Steel Science 2024, 2024, pp. 189–192, https://doi.org/10.2355/isijisss.2024.0_189.
[42] H. Fuchigami, H. Minami, M. Nagumo, Effect of grain size on the susceptibility of martensitic steel to hydrogen-related failure, Philos. Mag. Lett. 86 (2006) 21–29, https://doi.org/10.1080/09500830500482316.
[43] S. Takaki, K.-L. Ngo-Huynh, N. Nakada, T. Tsuchiyama, Strengthening mechanism in ultra low carbon martensitic steel, ISIJ Int. 52 (2012) 710–716, https://doi.org/10.2355/isijinternational.52.710.
[44] S.C. Kennett, G. Krauss, K.O. Findley, Prior austenite grain size and tempering effects on the dislocation density of low-C Nb–Ti microalloyed lath martensite, Scr. Mater. 107 (2015) 123–126, https://doi.org/10.1016/j.scriptamat.2015.05.036.
[45] S. Morito, H. Yoshida, T. Maki, X. Huang, Effect of block size on the strength of lath martensite in low carbon steels, Materials Science and Engineering: A 438–440 (2006) 237–240, https://doi.org/10.1016/j.msea.2005.12.048.
[46] Y. Momotani, A. Shibata, D. Terada, N. Tsuji, Effect of strain rate on hydrogen embrittlement in low-carbon martensitic steel, Int. J. Hydrogen Energy 42 (2017) 3371–3379, https://doi.org/10.1016/j.ijhydene.2016.09.188.
[47] Y. Momotani, A. Shibata, T. Yonemura, Y. Bai, N. Tsuji, Effect of initial dislocation density on hydrogen accumulation behavior in martensitic steel, Scr. Mater. 178 (2020) 318–323, https://doi.org/10.1016/j.scriptamat.2019.11.051.
[48] S.K. Banerji, C.J. McMahon, H.C. Feng, Intergranular fracture in 4340-type steels: effects of impurities and hydrogen, Metall. Trans. A 9 (1978) 237–247, https://doi.org/10.1007/BF02646706.
[49] K. Okada, A. Shibata, N. Tsuji, Characteristics and formation mechanism of serrated markings on the hydrogen-related quasi-cleavage fracture in as quenched low-carbon martensitic steel, Scr. Mater. 234 (2023) 115568, https://doi.org/10.1016/j.scriptamat.2023.115568.
[50] Jr. Morris John William, On the ductile-brittle transition in lath martensitic steel, ISIJ Int. 51 (2011) 1569–1575, https://doi.org/10.2355/isijinternational.51.1569.
[51] J.W. Morris Jr., C. Kinney, K. Pytlewski, Y. Adachi, Microstructure and cleavage in lath martensitic steels, Sci. Technol. Adv. Mater. 14 (2013) 014208, https://doi.org/10.1088/1468-6996/14/1/014208.
[52] A. Shibata, T. Katsuno, M. Tsuboi, N. Tsuji, Effect of bain unit size on low-temperature fracture toughness in medium-carbon martensitic and bainitic steels, ISIJ Int. 64 (2024) 381–388, https://doi.org/10.2355/isijinternational.ISIJINT-2023-141.
[53] A. Shibata, Y. Madi, J. Besson, A. Nakamura, T. Moronaga, K. Okada, I. Gutierrez-Urrutia, T. Hara, Relationship between three-dimensional crack morphology and macroscopic mechanical properties of hydrogen-related fracture in martensitic steel, ISIJ Int. 64 (2024) 660–667, https://doi.org/10.2355/isijinternational.ISIJINT-2023-316.